Thermal annealing and hydrogen exposure effects on cluster-assembled nanostructured carbon films embedded with transition metal nanoparticles

R. G. Agostino,* T. Caruso, G. Chiarello, A. Cupolillo, D. Pacilè, R. Filosa, V. Formoso, E. Colavita, and L. Papagno
INFM-Dipartimento di Fisica, Università della Calabria, Ponte Bucci, Cubo 33c, I-87036 Arcavacata di Rende (CS), Italy

C. Ducati
Department of Engineering, University of Cambridge, Trumpington Street, Cambridge CB2 IPZ, United Kingdom

E. Barborini, C. Lenardi, G. Bongiorno, P. Piseri, and P. Milani
INFM-Dipartimento di Fisica, Università di Milano, via Celoria 16, I-20133 Milano, Italy
(Received 17 January 2003; published 16 July 2003)

We have studied the morphology and electronic structure of cluster-assembled carbon films containing nickel and titanium nanoparticles by structural probes (transmission electron microscopy) and electronic spectroscopies (x-ray absorption, Auger spectroscopy, and electron energy loss). Vibrational characteristics of the surface have been investigated using high resolution electron energy loss spectroscopy. Nanocomposite carbon-metal films have been grown by supersonic cluster beam deposition of carbon clusters produced in the presence of finely dispersed metal catalysts. Characterization has been performed on pristine, annealed (at 560 K in vacuum), and H_2 exposed ($p_{H_2}=1$ mbar) samples. The nanocomposite films are characterized by metallic clusters embedded in a matrix of nanostructured carbon. The carbon structure at the nanoscale depend upon the type of metallic species. The electronic properties of the as-deposited films do not show any evidence of carbide formation. Thermal treatment and H_2 exposure procedures have different effects on the electronic features inducing a certain degree of bond ordering and a decrease of the available sp^2 sites, respectively.

DOI: 10.1103/PhysRevB.68.035413 PACS number(s): 81.05.Zx, 73.22.Lp

I. INTRODUCTION

Nanostructured carbon-based solids are attracting an increasing interest for the ever-growing variety of structures, forms, and functions that one can find in these systems. Moreover nanostructured carbon has shown promising properties for wide range of applications in electrochemistry, catalysis, gas sensing and storage.[1] One of the most puzzling aspects of nanostructured carbon is the capability of forming different isomers and structures starting from a common plasma state.[2] The control of the formation mechanisms in order to produce materials with tailored structure and functions remains a tremendous scientific and technological challenge. The use of metal atoms or clusters as catalysts for the controlled growth of nanotubes, onions and other types of carbon nanostructures is widely used and it is considered ready for niche industrial applications.[3–5] A very large number of studies have been devoted to the morphological characterization of carbon nanostructures containing or grown in the presence of metallic species.[6,7] Much less attention has been directed to characterize the modification induced by the presence of metallic particles on the physicochemical properties of nanostructured carbon-based systems. Several physical and chemical methods are currently used for the production of carbon nanotubes in the presence of metallic nanoparticles.[7] Arc discharge and laser ablation starting from targets containing a metallic precursor are very popular for the production of carbon nanotubes.[7] The main drawbacks are the complicate procedure of nanotube purification from metallic nanoparticle and from other carbon debris and the relatively high cost of the purified material.[8] Moreover the structural and functional properties of the final products are very difficult to control on a large scale with the precision necessary for very demanding applications such as microelectronics. Hydrogen storage is an application where a very precise control of nanotube features such as length, chirality, presence of defect is not critical, however the presence of metallic impurities in the final product can make very difficult a precise study of the storage properties of the nanotube-based material.[9,10] On the other hand, to turn a vice into a virtue, the controlled inclusion of metallic nanoparticles could improve the hydrogen storage capabilities or, more generally, the electrochemical activity, and hence make the metal-carbon nanocomposite material interesting for various applications.[11] Supersonic cluster beam deposition (SCBD) has been demonstrated to be a powerful tool for the synthesis of nanostructured and nanocomposite carbon-based materials.[12,13] In particular it has been shown that it is possible to produce nanostructured carbon films with controlled structure and topology by inserting during the carbon cluster growth metallic precursors. Depending on the chemical composition, dimension and density of the metallic nanoparticles, the cluster-assembled films have characters ranging from a negatively curved spongelike structure[12] to and amorphous matrix embedding nanotube embryos and onions.[13] In the present study we investigate the structural, electronic and vibrational characteristics of nanostructured carbon films containing transition metal nanoparticles. We have chosen a production method in order to deposit films containing carbon cage particles and metallic clusters embedded in an amorphous matrix. In particular we have focused our attention on the structural and electronic modification induced by thermal annealing and exposure to molecular hydrogen.

II. EXPERIMENT

A detailed description of the cluster beam deposition apparatus and of the working principle of a pulsed microplasma cluster source (PMCS) has been reported elsewhere.[14] Here we briefly describe the PMCS operation with particular attention to the introduction of metallic precursors in order to obtain nanocomposite thin films. The formation of the supersonic cluster beam starts with the injection of a helium pulse into the reaction chamber of the source by means of a solenoid pulsed valve. This helium jet is directed towards a graphite target rod. A pulsed electric discharge ionizes the gas forming a plasma confined by aerodynamic effects. The plasma erodes the target on a well-defined spot, the sputtered atoms thermalize with the helium bath, condense into clusters that are carried by helium through the PMCS nozzle to form a supersonic expansion. The cluster beam is then deposited on a substrate intersecting the supersonic beam.

To produce a carbon-metal nanocomposite we have used a mixed target rod formed by two graphite cylinders separated by a thick metal disk. Since the target erosion process is highly localized and controllable,[14] we can sputter the metal-graphite border region eroding at the same time carbon and metal. For the experiments reported here we have used a mixed target made with nickel or titanium (purity 99.99+%).

The samples have been grown on silicon and aluminum substrates with the same working parameters of the source. After the deposition process, the erosion of both components of the target (larger for the graphite) has been observed. This represents an indication of metal inclusion in the films, subsequently confirmed by energy dispersive analysis (EDX). Respect to carbon, the amount of Ni and Ti in the corresponding sample is comparable. The measured thickness of the nanostructured films containing nickel Ni:ns-C was $\sim$300 nm and of those containing titanium Ti:ns-C was about $\sim$700 nm.

Nanocomposite films have been characterized by transmission electron microscopy (TEM),[15] near-edge x-ray absorption fine structure spectroscopy (NEXAFS),[16,17] Auger electron spectroscopy (AES), electron energy loss spectroscopy (EELS), and high resolution electron energy loss (HREELS).[18,19]

TEM micrographs have been taken with a microscope Jeol JEM 4000EX, 400 kV. The NEXAFS experiments have been carried out at LURE Super-ACO storage ring on the beamline SA72 equipped with a high energy 10 m TGM monochromator (200–800 eV), with energy resolution of 0.2 eV at the carbon *K* edge. The spectra have been acquired in total electron yield (TEY) mode. The depth sensitivity was about 100 Å. The NEXAFS signal is obtained by the ratio between the signal given by the channeltron collecting electrons coming out from the sample and the intensity of the incident beam get by the photoinduced current in a 85% transmission gold coated grid placed downstream the exit slit. The AES, EELS, and HREELS measurements, as well as the NEXAFS measurements, have been performed *ex situ* in a ultrahigh vacuum chamber with a base pressure of 10^{-10} mbar. The chamber was equipped with a high-resolution measurement stage formed by an angular resolved hemispherical analyzer (50 mm mean radius) and by an electron gun with hemispherical lenses producing monochromatic electron beams with energy resolution up to 10 meV and a primary electron beam energy ranging from 0 to 300 eV. The HREELS measurements have been carried out in specular geometry using a 25.0 eV primary electron beam with a FWHM equal to 28.0 meV. The AES spectra were taken in a second stage placed in the same UHV chamber in a sector adjacent the high resolution one. AES spectra are produced by electron beam impact with energies ranging from 700 to 3500 eV and recorded by means of an electron hemispherical analyzer (100 mm mean radius). The sample holder is equipped with a resistive heating system and a sample temperature probe (K thermocouples). The apparatus was equipped with a pure-gas inlet system connected to a hydrogen bottle (6.0 purity grade). Before characterization the samples are inserted in the UHV chamber and successively, following the normal ''bake-out'' procedure, the system temperature is maintained at 420 K in UHV conditions for 24 h. We have characterized the effects induced by thermal treatment up to 560 K for 180 s in UHV and successively exposed to a high dose of H_2 molecules (3600 s, $p_{H_2}=1$ mbar, $T_{sample}=295$ K). During the annealing process the system pressure is kept below 5×10^{-8} mbar.

III. CHARACTERIZATION OF NONTREATED SAMPLES

In this section we analyze structural and electronic properties of the pristine films. The structure at nanometer scale has been investigated by transmission electron microscopy while the electronic properties by x-ray absorption and Auger spectroscopy. Other results on nontreated samples have been also obtained with EELS and HREELS. However, they will be presented in the next section because they are directly compared and correlated to the data of the samples annealed and exposed to hydrogen.

A. Nanoscale structure

TEM analysis shows, in both the case of Ni and Ti inclusions, that the nanoscale structure of the films is characterized by the presence of three main features: (i) nanosized metal particles; (ii) ordered graphitic nanostructures (such as onions and nanotube embryos); (iii) distorted graphene sheets and generically amorphous carbon. Examples of these typical features are shown in Figs. 1 and 2 for Ni and Ti, respectively. Diffraction images and evaluation of the lattice spacing indicate that carbides are not formed nor interstitial carbon atoms in the metal nanoparticle lattice are present: at the end of the synthesis route, carbon species and metal species appear to be separated. This is expected in the case of Ni, however, it is somehow surprising in the case of Ti, whose tendency to form carbides is well known.[20] The amount of ordered graphitic nanostructures in the films appears to be related to the metal species: in the case of Ni the number of these structures is much larger than in the case of Ti. Undoped nanostructured carbon films already contains a certain amount of such ordered graphitic structures, shown in

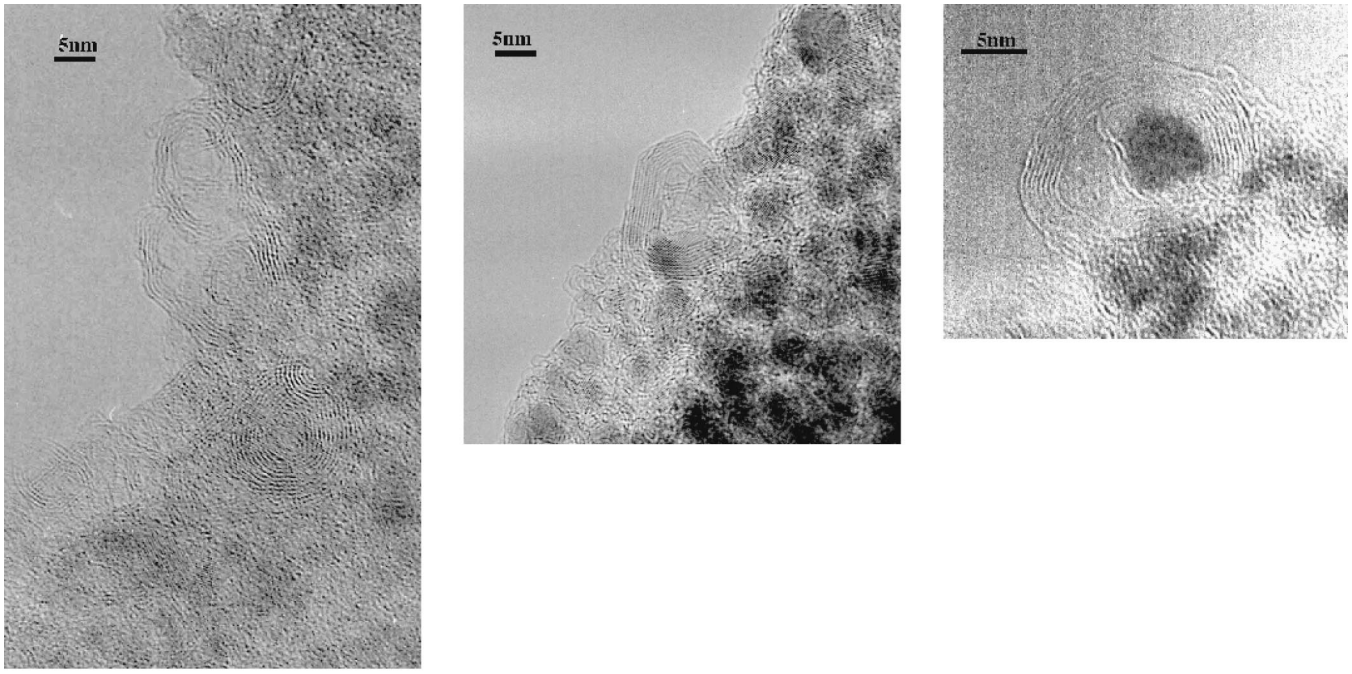

FIG. 1. TEM images of Ni:ns-C films: (a) dense distribution of ordered carbon nanoparticles mainly showing onion-like structure. A few of them are composed by several layers, as the one placed in the center of the micrograph which shows 12 layers; (b) uniform distribution of nanosized nickel particles (dark areas, shorter lattice spacing) embedded in the carbon matrix; (c) detail of a metal particle surrounded by equally spaced graphitic shells.

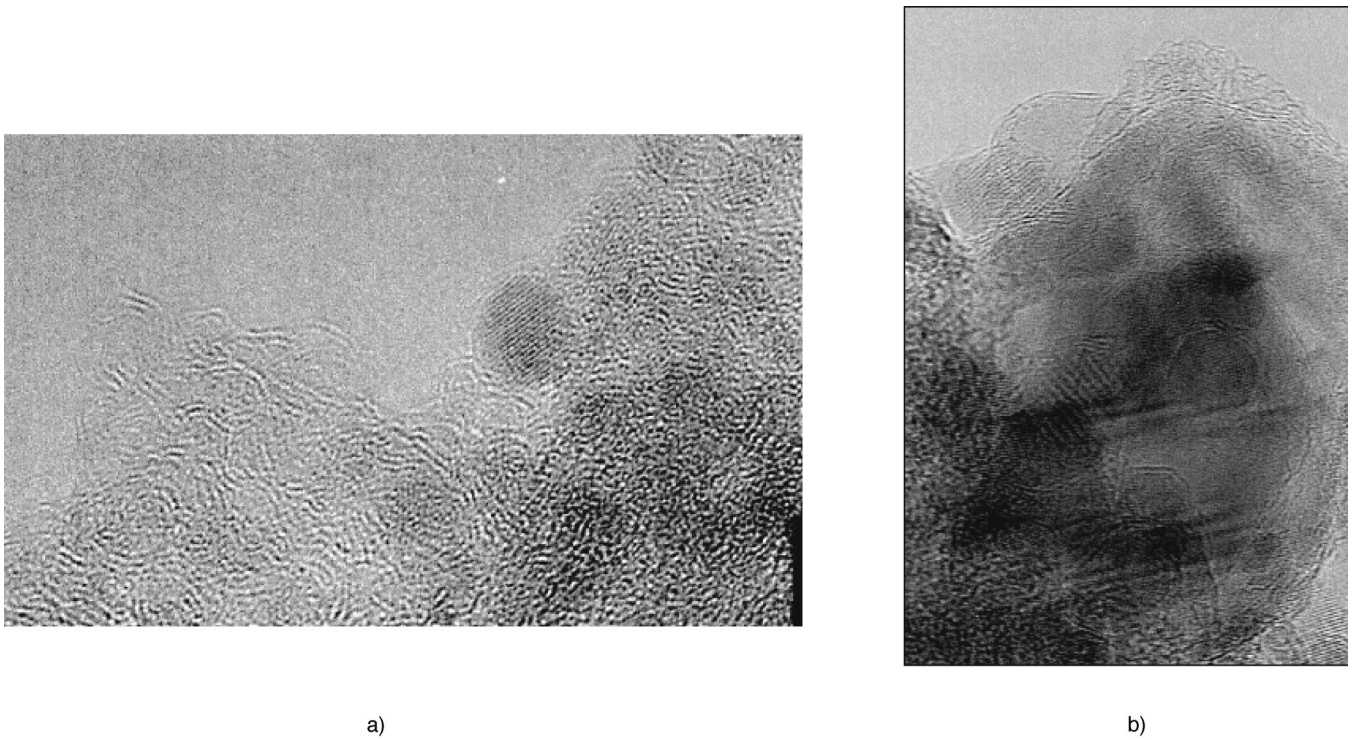

FIG. 2. TEM images of Ti:ns-C films: (a) distribution of titanium clusters (ordered particles) embedded in amorphous carbon and distorted graphene sheets; (b) wide sized titanium particles covered by graphitic layers.

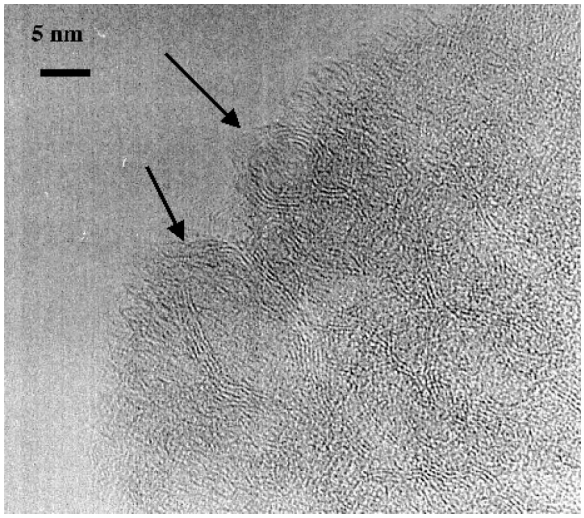

FIG. 3. TEM image of ns-C film: the arrows indicate ordered carbon structures also contained in less amount in undoped films.

Fig. 3, as spontaneous result of gas phase carbon atoms assembling. Our observation indicates that the presence of Ni favors the synthesis route towards ordered structures, while Ti seems to inhibit it. As shown in Fig. 1(a), the Ni-incorporating material is rich in onionlike structures, some with up to more than ten graphene layers, uniformly distributed across the samples. On the contrary, Ti containing films are poor in these structures and show predominantly a large fraction of highly distorted graphene sheets together with amorphous material [see Fig. 2(a)]. Ni particles are uniformly spread across the sample and have a spheroidal shape with a diameter in the range 2–7 nm. Most of these particles are covered by several graphitic shells, as shown in Fig. 1(b)–1(c). Ti particles have a wider size distribution than Ni, ranging up to about 50 nm. In most cases Ti particles are covered by 1 or 2 graphitic layers [see Figs. 2(a), 2(b)].

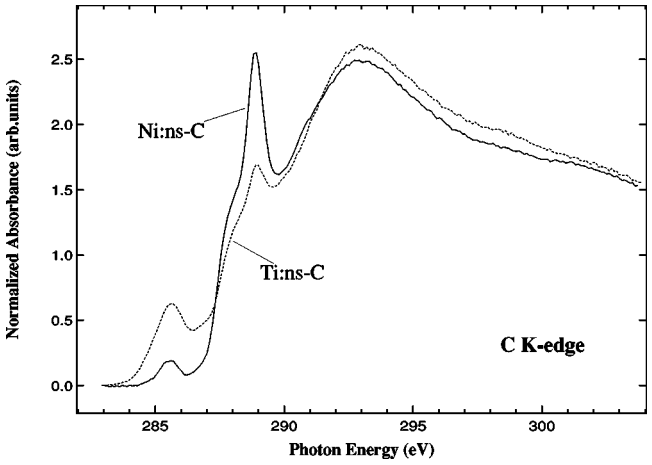

FIG. 4. NEXAFS spectra at the carbon *K* edge of the metal doped films. The Ni:ns-C films show a smaller content of sp^2 hybridized carbon, related to the $\pi^*_{C=C}$ resonance at ~285.5 eV. This reduced abundance of sp^2 sites is mainly due to the favored formation of bonds between carbon and hydrogen, as the larger intensity of σ^*_{C-H}~289.0 eV peak indicates.

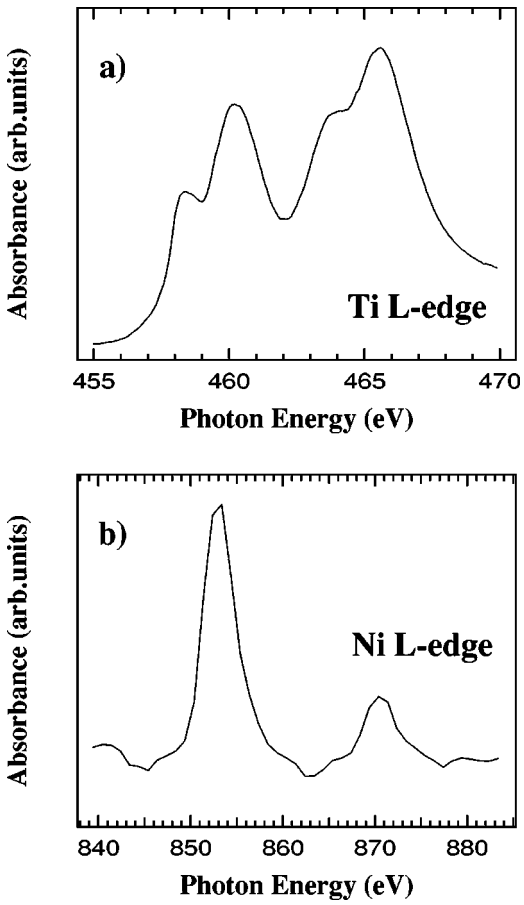

FIG. 5. NEXAFS spectra at the *L* edge of titanium (a) and nickel (b). The Ti:ns-C spectra show a strong oxidation of titanium (mainly, TiO_2), whereas there is no manifest contribute from a carbide component. In the Ni:ns-C the metallic nature of the nickel appear to be dominant.

B. NEXAFS spectra

The NEXAFS spectra have been acquired at the carbon and oxygen *K* edge, the titanium *L* edge, and the nickel *L* edge (second harmonic). In Fig. 4 the normalized spectra of Ni:ns-C and Ti:ns-C at the C *K* edge are reported. The spectra show two main features in the preedge region. The first one corresponds to $\pi^*_{C=C}$ resonance at 285.5 eV and is representative of the abundance of sp^2 hybridized carbon atoms and the second one at 289.0 eV is the $\sigma^*_{C\text{-}H}$ resonance, which indicates the presence of bonds between carbon and hydrogen. A relevant chemisorption of hydrogen in nickel containing films is disclosed by the presence of a strong $\sigma^*_{C\text{-}H}$ peak. Thus the inclusion of nickel appears to favor the absorption of hydrogen with a concomitant reduction of the available sp^2 sites, as the decrease of the π^* peak indicates. There is no evidence of the formation of titanium carbide, which would lead to a shift of the π^* peak towards higher energy[21] and the Ti:ns-C spectrum seems to resemble typical spectra of nanostructured carbon films.[22] A strong oxidation of the titanium can be evidenced at the Ti *L* edge, shown in Fig. 5(a). It is well known that the Ti *L*-edge features are very sensitive to the local bonding environment and in particular

to the oxidation states of Ti.[23] Normalized NEXAFS spectra show the dependence of the intensity and the line shape of the absorption peaks on the *d* occupancy in the oxide.[24,25] Our spectrum well resembles the profile of TiO_2,[23] where the doublet peaks split into two well-resolved features. The t_{2g} and e_g orbitals arise from the ligand-field splitting with an energy separation of 1.8 eV either for L_{III} and L_{II} peak. Also in the oxygen *K*-edge spectrum (not shown) the splitting can be detected ($\Delta E = 2.4$ eV). The *L*-edge of Ni is shown in Fig. 5(b), with a L_{III} and L_{II} spin orbit splitting of 17.0 eV. Neither multiplet structure nor energy shift as a fingerprint of oxidation are observed. Moreover the skewed shape of the peaks is a further indication of the prevalent metallic nature of the Ni particles embedded in the ns-C film.[26]

C. Auger electron spectra

Elemental composition of the films has been carried out by extended Auger spectra in $\Delta E = \mathrm{const}$ mode. This investigation shows signals coming from C, O, and metal atoms. No other elements are detected and, in particular, no nitrogen signal is revealed suggesting that the nitrogen at the surface content is below the AES sensitivity limit (1%). Previous works[27,28] report a homogeneous oxygen contamination of the ns-C films produced by the same growth technique and examined *ex situ*. This should be due to chemisorption of water, CO, CO_2 and oxygen molecules during the exposure to air. Vibrational spectra acquired by HREEL (see below) give evidence of C–H bonding but not of O–H and C–O bonding in all the examined films before and after any treatment. We, thus, exclude that water, CO and CO_2 molecules remain bonded in UHV conditions to the surface of the studied ns-C film.

A detailed line shape analysis of the Auger emission signals provides information on the chemical bonding of the films.[29–32] The emission maximum position at 254.0 eV, see Fig. 6, is consistent with C–C bond with both sp^3 and sp^2 hybridization in an indefinite geometry as in amorphous carbon.[33] However, a more detailed analysis of the line shape is complicated by the variety of contributions to the *KVV* Auger emission. Each orbital subset of the valence band will contribute to the Auger emission as a convolution with the other orbitals taking into account their energy distribution and the hole-hole correlation energy.[29] In order to get useful indications, we divide the valence band states into two net subsets: the σ and π states. The C–C bonding in amorphous C samples shows different percentage of σ and π states depending on the hybridization, on the order degree and on the H content.[34] The termination of the C dangling bonds with H results in a reduction of the π states and an apparent abundance of σ states due to the energetic similarity between the C $2p$ local density of states in C–H bond and the C $2p\sigma$ states in C–C bonds.[29] In general, in amorphous C the π states binding energy average is always lower than that of σ states even though a net energetic separation between π and σ bonds does not hold. As a matter of fact, the *KVV* emission from graphite, diamond and carbides is structured while in amorphous C we find a smooth peak and the Auger line shape will result from the sum of several overlapping components. Nevertheless, the $\sigma^*\sigma$, $\sigma^*\pi$, and $\pi^*\pi$ emissions are placed in sequence at increasing kinetic energies in the 250–270 eV range. At higher energies we have the emission involving excitonic states and below 250 eV we find the shake-up contributions.[29]

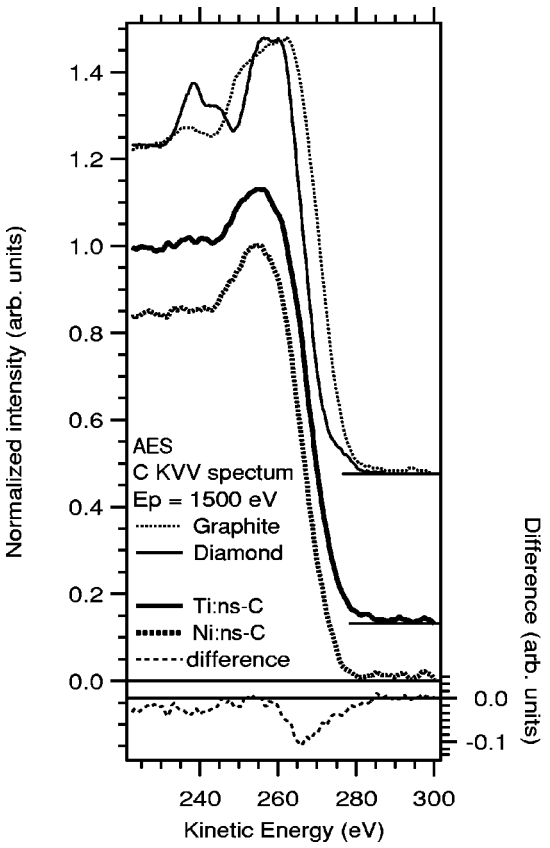

FIG. 6. Carbon *KVV* Auger emission spectra from Ni:ns-C and Ti:ns-C films induced by a primary electron beam with energy $E_P = 1500$ eV. The graphite (Ref. 32) and diamond (Ref. 30) spectra taken from literature are reproduced for comparison. The secondary electron background is fitted by a polynomial curve in the 287–300 eV energy range and then removed from the measured spectra. Successively, each spectrum is normalized to its maximum intensity. The bottom panel shows the difference spectrum of the normalized carbon *KVV* Auger emission spectra from Ni:ns-C and Ti:ns-C. The spectral difference shows a lack of intensity in the 260–275 eV range and below 243 eV. Note that the vertical scales are the same for the right and left axis.

We note that C *KVV* spectra of the nanocomposite films containing Ni and Ti present minor differences, as shown in Fig. 6. The resemblance of the line shapes indicates the close similarity of the local density of states around the C atoms and hence of type of bonding and ordering characteristics. The difference spectrum between the C *KVV* spectra of Ni and Ti samples reveals an intensity lack in 260–275 eV range of the former spectrum. In this region we find the $\sigma^*\pi$ and $\pi^*\pi$ contribution to graphite line shape and thus we ascribe this difference to an higher presence of unsaturated π bonds, belonging to carbon atoms in larger graphitelike networks, in the Ti film with respect to that one containing Ni in agreement with the NEXAFS findings.

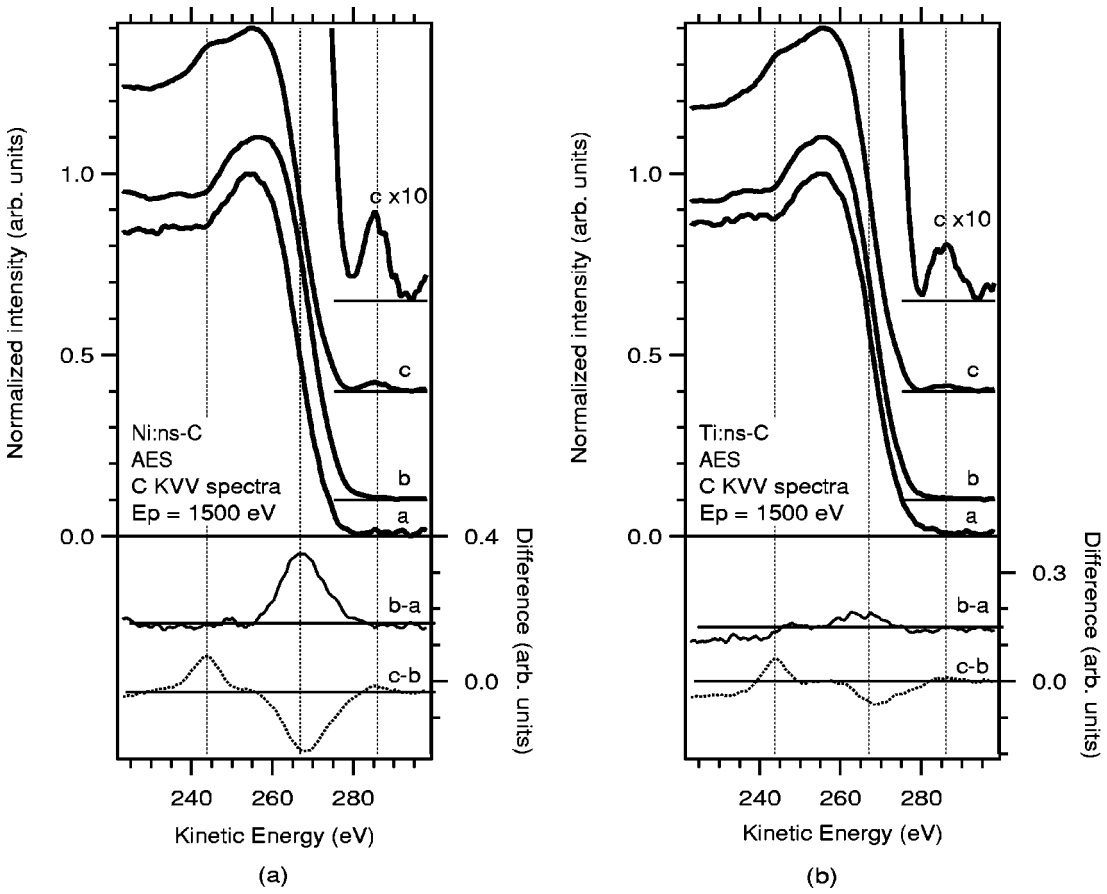

FIG. 7. Modification of the carbon *KVV* Auger emission induced by thermal treatment and H_2 absorption. (A) Ni:ns-C and (B) Ti:ns-C spectra showing the normalized line shape of (a) the pristine sample, (b) after 180 s at 560 K, and (c) 1 h at 1 mbar H_2, RT. An expanded view of the (c) spectra is placed on the top left of each panel. The bottom panels show the difference spectra to follow the modification induced by each treatment. Tiny dotted lines are traced to mark the energies where the major effects take place. Note that the vertical scales are the same for the right and left axis.

Furthermore a prevalence of sp^2 on sp^3 bonding is demonstrated by the presence in our spectra (see Fig. 6) of the typical emission in the kinetic energy range between 270.0 and 278.0 eV as in the C *KVV* spectra of graphite and graphitic compounds.[35] This signal is assigned to the transitions involving the valence $(\sigma+\pi)$ levels and the valence-core exciton.[31] that needs the presence of the excitonic levels in which the valence band electrons are localized.[36] In the low kinetic energy region it is located the emission given by another effect involving localized states, i.e., the shake-up transition, due to a dynamic screening effect of the hole-hole interaction in the final state.[31] In this region a plateau is present below 243.0 eV (see Fig. 6). The absence of a clear peak as in graphite[34] is probably due to the disorder in bonding configuration.

In conclusion, we find in the C network of the film containing Ti a larger amount of C–C bonds in a geometry similar to graphite and curved graphene surfaces, than in Ni film. In addition we find a lack of three distinct maxima as reported in C *KVV* spectra from metal carbide samples.[29] This is sufficient to directly exclude a strong diffusion of isolated metal atoms in the C network.

IV. THERMAL ANNEALING AND HYDROGEN EXPOSURE

In this section we will focus our attention on peculiar features of the C *KVV* spectra, EELS and HREELS spectra in order to identify the variation in the electronic structure of the film induced by in vacuo annealing and H_2 exposure.

A. Carbon *KVV* spectra

Thermal treatment (180 s at 560 K) changes the carbon *KVV* line shape for both Ni- and Ti-containing films, as shown in Figs. 7(a) and 7(b). The modification could be related to the removal of weakly bonded species from the surface and/or to an induced bonding rearrangement. In order to gain a deeper understanding of the annealing effects, we have studied the spectral differences and tried to correlate them with possible structural changes. A clear intensity increment in the 260–275 eV range with a maximum at 266 eV is present in Ni:ns-C spectrum while in Ti:ns-C one we observe a similar but weaker enhancement [see curves (b)–(a) in the bottom panel of Fig. 7]. As discussed above, the 260–275 eV energy range is occupied by $\sigma^*\pi$ and $\pi^*\pi$ contribution to graphite line shape. This confirms that in the Ni:ns-C sample the presence of molecules weakly chemical

bonded to the surface which are desorbed upon annealing at 560 K. This finding is in agreement with previous studies on different pure C composites,[37–39] demonstrating that the desorbed species are C_nH_m fragments. Electronic structure calculations on amorphous carbon[40] show that the rise of the π orbitals energy after removal of adsorbed species, could result in an ordering process. In fact, the π bonding energy is maximized by the formation of $\sim$20 Å graphite island.[40] Following this study, the internal strain is relieved by the formation of sp^3 bonding at the island edges. Our findings, i.e., a clear and energetically defined increase of the π-related feature in the C *KVV* emission, are consistent with this hypothesis, i.e., we get a hint on possible graphite islands formation in the Ni:ns-C film. This phenomenon assumes different behavior in the Ti:ns-C sample remarking the different catalytic effects of the inclusion of the two metal clusters. The slight increase of an already intense emission in the π-related region confirms that those states are already present in the film before the thermal treatment. At this point, we may trace an overall image of the annealed ns-C films: flat graphiticlike surfaces are present in the film and on top of the multiwall carbon coating of the metal clusters while the most of the carbon network is formed by sp^2-bonded atoms in a distorted geometry. Highly curved carbon surfaces enclose the metal particles and, probably, are also present in the film. Only few carbon atoms, mainly placed at the border of flat and curved carbon surfaces, are sp^3 hybridized.

Major changes in the AES spectra are evident after an exposure to high dose of molecular hydrogen (3.6×10^9 Langumir, $p_{H_2}=1$ mbar at $T=295$ K) in both Ni- and Ti-containing films [curve c in Figs. 7(a) and 7(b)]. A strong depletion of the emission in the 260–275 eV range occurs associated with the rise of a new structure at 243.0 eV, on the low kinetic energy side of the main peak placed at 254.0 eV. The first effect is the opposite of that observed upon annealing of the pristine films. Following the same argumentation of the previous paragraph, we assign it to the removal of π bonding by H adsorption. We guess that the adsorption process takes place in the sp^2 network and on the border of the graphite islands and highly curved carbon surfaces but not on top of them as shown by several hydrogen adsorption studies on graphite samples.[37] As already noted, the energy position of the valence band states of the C–H bonding is similar to that of the C–C σ bonding although with a higher binding energy with respect to π orbitals.[34,40] The emerging of the 243 eV structure is determined by the presence of those new valence band states. However, its energy position is shifted to lower kinetic energy with respects to σ-σ emission in the C–C bond. This has to be related to an increase of the hole-hole repulsion in the C *KVV* final state considering C–H valence states instead of C–C ones, caused by their stronger localization.[41] The fact that in the Ni:ns-C spectrum the H-induced effects are larger show how the thermally activated absorption states in this film are more reactive of those present in pristine Ti:ns-C films.

An interesting satellite, with a well-defined shape and low intensity, appears in both films after the H- exposure on the high kinetic energy side of the *KVV* line shape base at 285.0 eV [see the scaled-up curve c in Figs. 7(a) and 7(b)]. Emissions at so high kinetic energy could have two opposite origins: it could involve highly delocalized and weakly bonded valence-band states, i.e., be related to an enhancement of a free-electron-like density of state around the Fermi level, or, alternatively, it could be due to resonant processes known also as autoionization emission.[29,41–43] The autoionization process, accessible only by electron excitation, needs the presence of localized electrons in an excitonic or bound state upon creation of a core hole.[41] We consider the second hypothesis as more probable and in this case it should be due to the availability of new C–H* localized states.[29] The localization of the C–H* states is a counterpart of the localization of the C–H states involved in the 243 eV emission feature. Another reason to exclude the first hypothesis is the measured decrease of π states that mainly contribute to the DOS close to the Fermi level.[40] If our interpretation is correct this should be the first report on autoionization emission in electron excited Auger emission from C composites.

Conclusive notes on both desorption and H-adsorption processes could be traced looking to the wide range AE spectra (not shown). The Auger peaks relative to C *KVV*, O *KVV*, and Ti $L_{23}VV$ in the Ti:ns-C film do not show any significant variation upon annealing and H_2 exposure apart from a tiny decrement (-5%) of the C *KVV* signal after the annealing procedure. On the other hand, in the Ni:ns-C film we find that the O *KVV* and Ni $L_{23}VV$ signals remain constant while C *KVV* intensity reduces to half upon annealing. An explanation of the different behavior upon annealing at 560 K of Ti:ns-C and Ni:ns-C films could be assigned to a more consistent desorption of C_nH_m fragments from Ni:ns-C film with respect to Ti:ns-C film. In fact, at RT the H atoms present in the film form strong covalent bonds terminating the C dangling bonds. In order to reduce the C content it is necessary a heating treatment above 570 K which stimulate the desorption of C_nH_m radicals from the surface in C nanostructured composites.[37]

B. Electron energy loss spectra

In Fig. 8 we show the EEL spectra acquired in correspondence to the AES spectra. All spectra are characterized by two structures separated by a loss minimum at 8.1 eV. A double peak, placed between 1.0 and 8.1 eV, is associated to plasmon excitation involving the π electrons of the nanostructured carbon. The intensity of the low energy plasmon loss in C allotropes is generally associated to π collective excitation and reaches its maximum in graphite EEL spectra.[34,44] as shown in Fig. 9. The π plasmon excitation in graphite is revealed by a single peak at 6.6 eV and it is totally absent in diamond spectra.[34,44] Moreover, EEL spectra obtained from both carbon nanotube and fullerene samples, show a double structure for energy losses similar to those observed in our film apart from a slight shift to higher energy loss in the nanotubes samples.[44,45] In the case of fullerenes and nanotubes, the structure is attributed to plasmon excitation of π electrons whose degeneracy is removed by sp^2 bonding dissimilarity in the C network and, consequently, different plasma energies are observed.[44] In both sp^2 - and

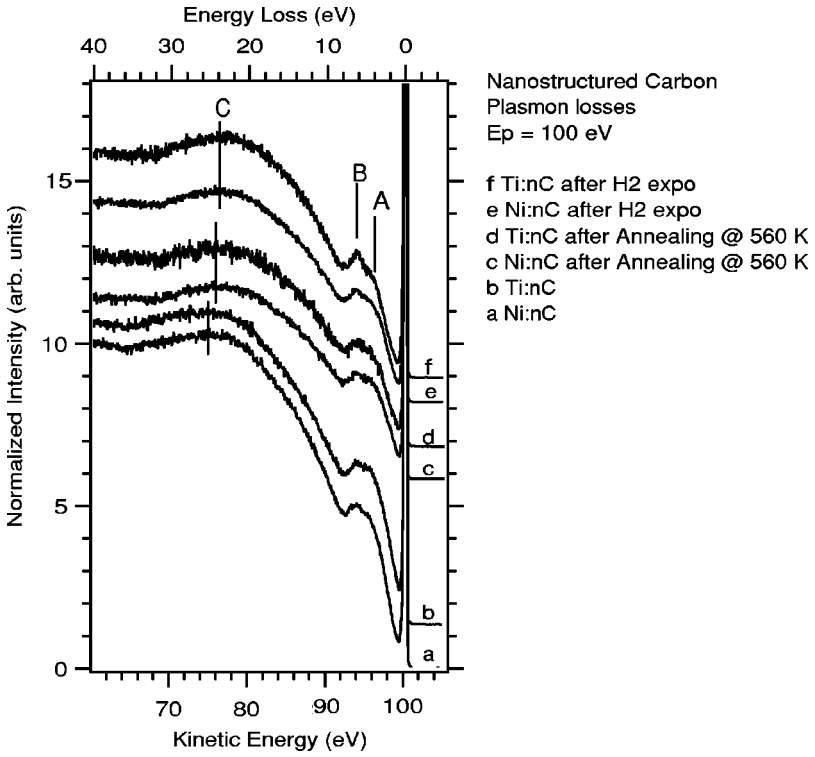

FIG. 8. Collection of the electron energy loss spectra collected at a primary energy of 100 eV. The panel shows the evolution of the plasmon loss region after thermal treatment and H_2 exposure. Each spectrum normalized to the elastic peak intensity maximum and successively aligned to the elastic peak position in order to get a common energy loss scale (upper axis). Labels A and B mark the π-plasmon loss while label C is related to $\sigma+\pi$ plasmon.

sp^3 -amorphous C the observed π-plasmon loss is very weak. The existence of an intense double structure in our spectra as in fullerenes and nanotubes, allows us to confirm the hypothesis that nanometer-scale curved surfaces are embedded in the carbon network. Those structures are mainly composed by distorted sp^2 bonds. In our EEL spectra we can evaluate the relative intensity of the two components and its variations as consequence of thermal treatments and hydrogen exposure to follow the evolution of the π-bonding related features. A curve fitting procedure performed using a double Gaussian peak superimposed to a linear background (see Fig. 10) allows the determination of the positions and FWHM of both peaks, labeled A and B. In Table I the results of the fitting for the Ni:ns-C spectrum after H_2 exposure are

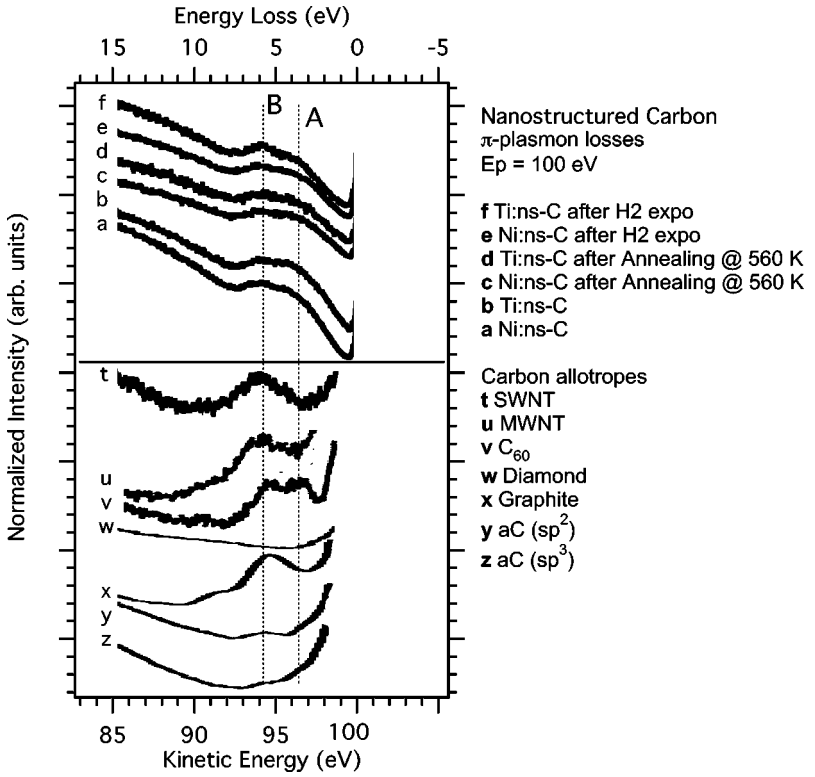

FIG. 9. Comparison of the collected spectra with the literature showing the π-plasmon energy loss region. C60, multiwall carbon nanotubes (MWNT) (Ref. 44), Diamond, graphite, a-C (Ref. 34) and single wall carbon nanotubes (SWNT) (Ref. 45) energy loss spectra are reproduced in order to find out similarities with the double structure of the π-plasmon loss shown by the ns-C spectra. Labels A and B mark the components of this loss features placed at 4.1 ± 0.2 and 6.4 ± 0.1 eV. Note the energy loss coincidence of peak B and π-plasmon loss in graphite.

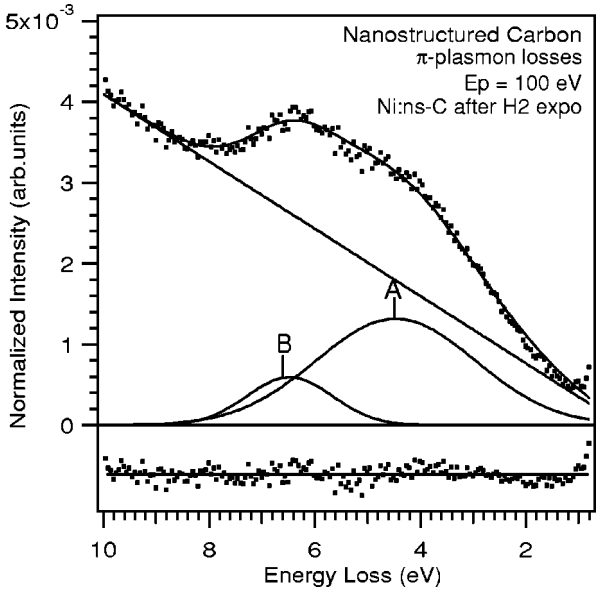

FIG. 10. Fitting procedure applied on the Ni:ns-C spectrum after H_2 exposure to evaluate energy loss position and energy spread of the A and B components of π plasmon loss. The obtained values are reported in Table I.

resumed. Peak B results to be energetically well defined while peak A, at lower plasmon energy, is broader and more intense. The energy loss of the B peak coincides with the π-plasmon loss in graphite and we expect that part of its intensity is due to graphite islands present in our films. The intensity ratio between B and A plasmon peaks is reported in Table II. The average intensity ratio is 0.24 ± 0.02 apart from the pristine Ni:ns-C result in which plasmon B has a lower intensity. This behavior has to be related to the AES results that show the rising of a graphitelike emission features upon annealing the Ni:ns-C sample and a much weaker effect in the Ti:ns-C sample. Thus, the increasing of the 6.4 eV plasmon loss intensity has to be interpreted in terms of the creation of graphite islands as a consequence of the annealing process in the Ni:ns-C sample. Furthermore, the higher intensity of the B peak in the pristine Ti:ns-C sample with respects to the pristine Ni:ns-C one, gives us further evidence of the existence of graphite islands in as prepared Ti-containing films. Once the graphite islands and highly curved C surfaces are formed, they do not evolve under annealing and H_2 exposure as demonstrated by the invariance of the $I(B)/I(A)$ ratio. This is in agreement with the conclusion of the AES analysis that showed how H absorption does not take place on top of those kind of structures.

The larger structure placed at energy loss higher than 8 eV is assigned to $\sigma+\pi$ plasmon excitation. From a close analysis of the data in the 8–40 eV range, we find that the main intensity maximum is placed at 26 eV in the pristine samples, shifts to 24 eV after thermal treatment at 560 K, shifting slightly to lower loss energy after hydrogen exposure. A shoulder at 14 eV is also present in Ni:ns-C spectra and at 13 eV in Ti:ns-C ones. The energy of the $\sigma+\pi$ plasmon $\hbar\omega_{\sigma\pi}$ is closely related to the hybridization, being 33.0 eV in diamond and 25.2 eV in graphite.[46] In amorphous C samples an increment of the sp^3 fraction results in a linear increase of $\hbar\omega_{\sigma\pi}$ between 23.0 eV (0% sp^3) to 31.5 eV (100% sp^3).[46] This behavior is related to the density dependence of the material on the hybridization,[47] i.e., to the steric volume occupied by the sp^2- and sp^3-C atoms. With a similar mechanism, the $\sigma+\pi$ plasmon energy has to be related to the H content, which in general decreases the amorphous C density.[47] The measured $\sigma+\pi$ plasmon energies are close to the minimum values in agreement with the expected prevalence of sp^2 bonding and a consequent low density. The observed negative $\hbar\omega_{\sigma\pi}$ shift upon annealing is related to the conversion of sp^3 to sp^2 bonds with a consequent increment of the volume. The explanation of the invariance of $\hbar\omega_{\sigma\pi}$ after the H exposure has a less straightforward explanation: in AE spectra we do observe a chemical reaction between H and the C film with a reduction of features related to the π levels. The C–H bond formation should determine a decrement of the density, i.e., a decrease of $\hbar\omega_{\sigma\pi}$, but this is not the case in our ns-C films.

TABLE I. Average energy position and spread of the π-plasmon A and B obtained after the fitting procedure described in the text.

	Energy Loss (eV)	FWHM (eV)
Plasmon A	4.1 ± 0.2	3.5 ± 0.7
Plasmon B	6.4 ± 0.1	1.9 ± 0.4

TABLE II. Ratio between the intensity of peaks B and A (π plasmons) as obtained from the fitting procedure.

	$I(B)/I(A)$ π plasmons intensity ratio	
Sample	Ni:ns-C	Ti:ns-C
Pristine	0.20 ± 0.01	0.23 ± 0.01
Annealed	0.25 ± 0.01	0.22 ± 0.01
H_2 exposed	0.24 ± 0.01	0.24 ± 0.01

C. HREELS

The vibrational spectra, shown in Fig. 11, present four peaks whose main characteristics of these peaks are summarized in Table III together with their identification on the basis of the current literature.[38,39,48,49] In order to closely study the energy loss positions, energy spread, and intensity variations of the measured peaks we adopted a fitting procedure in which each peak is simulated by a Gaussian curve and the inelastic background is simulated by negative exponential type curves. We clearly distinguish the C–C stretching mode that dominates the spectra at 102 meV (peak A) with a narrow FWHM. This mode is reported as a low-dispersion optical mode in graphite[50] and in carbon nanotube[45] and thus it is coming from the graphite islands and the distorted-sp^2 curved surfaces present in our samples. On the other hand, several components contribute to the large peak B placed at 150 meV. They are mainly attributed to C–C and C=C combined vibrational modes[38,39,49] in the carbon network and, in a minor extend, to CH_x bend and rocking modes. A comparison with nanotube vibrational

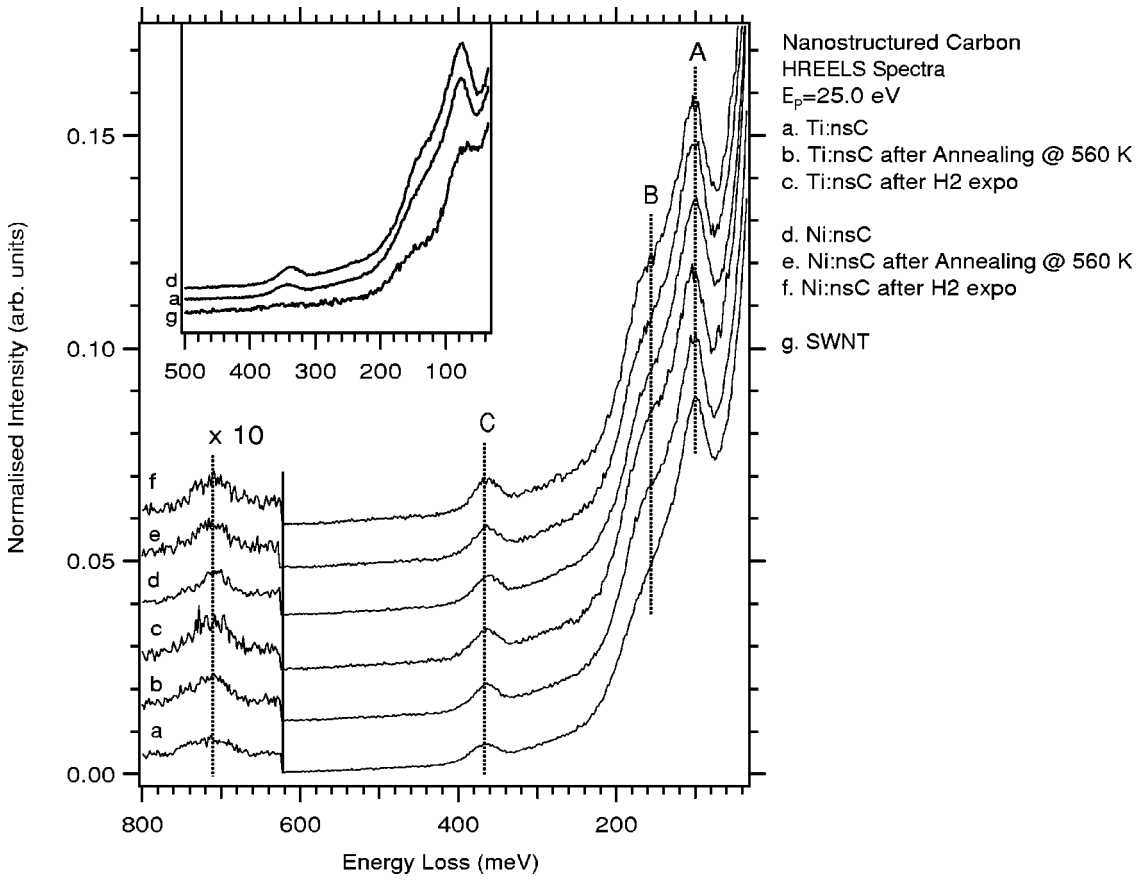

FIG. 11. Collection of the high resolution electron energy loss spectra collected at a primary energy of 25.0 eV with a spectral resolution of 30 meV. The panel shows the evolution of the vibrational loss region after thermal treatment and H_2 exposure. Each spectrum normalized to the elastic peak intensity maximum and successively aligned to the elastic peak position in order to get a common energy loss scale. Labels A, B, and C mark the C−C, mixed C−C, C−H, and C−H vibrational modes, respectively (see Table III). Tiny dotted vertical lines are placed to follow the intensity maxima position.

spectrum (inset of Fig. 11) allows us to distinguish between them assigning to the CH_x bend and rocking modes the less energetic contribution to the peak. Peak C, at 362 meV, is generally assigned to C–H stretching modes. Its energy position is compatible with a vibration between H and mixed sp^2/sp^3 carbon atom (see Table III), corroborating the hypothesis that H is bonded to C atoms in the C amorphous network and not to those forming the graphite islands. At 710 meV we find the overtone of the C–H stretching mode. The energy position and spread of all these structures do not vary over annealing and H_2 exposure in both Ti:ns-C and Ni:ns-C films. Unfortunately, due to the uncertain geometry of electron scattering on the surface, we are not in the appropriate condition to get meaningful relationships between the peaks intensity and the relative concentration of C–C and C–H bondings. The extreme simplicity of the spectra of Fig. 11 gives us a further series of hints on the status of the ns-C film surface and on the presence of molecules bond to it. As a first indication, we can deduce that C–H bonding is already present in the pristine sample as a consequence of the exposure to air,[51] and it is not removed by annealing at 560 K. Moreover, the lack of a ν(H-H) stretching vibration peak at 520 meV shows the absence of molecular hydrogen bonded to the ns-C surface.

No C–O vibrational modes are detected [($\nu(C=O)$ at 200 meV and ν(C–O) at 133 meV]. No water or oxygen molecular vibration modes (at 446–457 meV and 200 meV) are observed as well suggesting the the oxygen revealed by Auger spectroscopy has to be related with the oxygen content in the embedded metal clusters. The energy loss positions of the detected peaks do not depend on metallic nanocrystal content, thermal treatments, and hydrogen exposure.

V. CONCLUSIONS

In this work we have presented the first structural and electronic characterization of metal containing nanostructured carbon films synthetised via supersonic cluster beam deposition with a PMCS source. The metal precursors (Ni or Ti) have been introduced in the cluster beam by using a mixed carbon-metal cathode rod. The structural analysis of nanocomposite films has shown the formation of graphitic ordered cages embedding the metal particles. Spectroscopic data do not support the presence of carbides neither the presence of strong intermixing of carbon and metal atoms. The amount of onionlike nanostructures is larger in nanostructured films containing Ni where metal inclusions are small spheroids (mean radius 2–7 nm) densely and uniformly dis-

TABLE III. Energy and FWHM of the vibrational losses observed in the HREEL spectra on ns-C films. The excited vibrational mode for each peak is presented following the attribution made in Refs. 38,39,48,49.

Peak	Energy loss (meV)	FWHM (meV)	Mode	Description	Notes
					100 meV in C_6H_{12} ($-CH_2-CH_2-$ sequence)
A 102±2	38±3	υ(C−C)	C−C stretching vibration		
					114 meV in $CH_3-CH=CH_2$
			δ(C−C)	C−C and C=C combined modes	
			δ(C=C)		contributions in the
B	150±7	79±10			
			δ(H−C−H)	CH_3 deform. (CH_2 scissor)	150-195 meV range
			(C−H)	C−H bending	
					376 meV in sp^2 C
					359 meV in sp^3 C
C	365±1	36±2	υ(C−$H_{s,a}$	CH_x (x=1, 2, 3) symmetric and asymmetric stretching	359 meV in sp^3 C
					339 meV in sp^3 C/Pt
					362 meV in a-C:H
			Overtone of		
D	710±4	58±5			
			υ(C−$H_{s,a}$) mode		

tributed in the carbon matrix. Ti:ns-C films present a wider size distribution of the metal clusters with larger nanoparticles (up to 50 nm) surrounded by distorted graphene sheets. The local coordination investigated by NEXAFS spectroscopy indicates a non-negligible ability of the Ni:ns-C films to chemisorb hydrogen and a related decrease of the available sp^2 sites. Electron spectroscopy data suggest several similarities and few interesting differences between the Ni:ns-C and Ti:ns-C films. Starting from the similar features we point out that Auger and electron energy loss data are consistent with a description of the local structure of ns-C films in terms of graphite islands and highly curved surfaces embedded in an amorphous carbon network with C atoms in sp^2 hybridization and, in a minor extend, sp^3 hybridization. Graphite islands are formed during the film growth in Ti:ns-C film and after a thermal treatment in Ni:ns-C. Once graphite islands are formed, they do not evolve under annealing at 560 K and H_2 exposure in both films. No trace of metal atoms diffusion in the carbon network during the film preparation process is found. Concerning the molecular content in the films we established that no H_2, water, N_2, CO, and CO_2 molecules remain bonded to the ns-C surface in UHV conditions. Only H atoms remain bonded to the film surface. In fact, our vibration signal reveals H terminated C bonds that are not altered by annealing at 560 K. On the other hand, the oxygen signal revealed by Auger spectroscopy has to be related with the oxygen content in the embedded metal clusters. Upon thermal treatment we find a more consistent desorption of C_nH_m fragments from Ni:ns-C films with respect to Ti:ns-C film. Both ns-C films react with H_2 molecules at RT and $p_{H_2}=100$ Pa giving rise to localized C–H and C−H* orbitals; the C–H bonds are formed in the amorphous carbon network and not on the graphite islands or on highly distorted carbon surfaces. Finally, we report an observation of autoionization emission at 286 eV in condensed phase carbon material in the AE spectra acquired after H_2 exposure; the effect is triggered by the existence of localized C−H* orbitals.

ACKNOWLEDGMENTS

The authors wish to thank S. Abate and G. Desiderio for their skillful technical support. This work was supported by the University and Research Ministry Cofinanziamento 99 national project.

*Email address: agostino@fis.unical.it

[1] *Nanostructured Carbon for Advanced Applications* edited by G. Benedek, P. Milani, and V. G. Ralchenko, Vol. 24 of NATO Science Series II: Mathematics, Physics and Chemistry (Kluwer Academic Publishers, Dordrecht, 2001).

[2] R.E. Smalley, Mater. Sci. Eng., B **19**, 1 (1993).

[3] S. Iijima and T. Ichihashi, Nature (London) **363**, 603 (1993).

[4] D.S. Bethune, C.H. Kiang, M.S. deVries, G. Gorman, R. Savoy, J. Vazquez, and R. Beyers, Nature (London) **363**, 605 (1993).

[5] M.J. Bronikowski, P.A. Willis, D.T. Colbert, K.A. Smith, and R.E. Smalley, J. Vac. Sci. Technol. A **19**, 1800 (2001).

[6] M. S. Dresselhaus, G. Dresselhaus, and P. C. Eklund, *Science of Fullerenes and Carbon Nanotubes* (Academic Press, New York, NY, San Diego, CA, 1996).

[7] See, for example, *Carbon Filaments and Nanotubes: Common Origins, Differing Applications?* edited by L. P. Biro, C. A. Ber-

nardo, G. G. Tibbetts, and P. Lambin, Vol. 372 of NATO Science Series II: Mathematics, Physics and Chemistry, (Kluwer Academic Publishers, Dordrecht, 2001).
[8] D. Chattopadhyay, I. Galeska, and F. Papadimitrakopoulos, Carbon **40**, 985 (2002).
[9] M. Ritschel, M. Uhlemann, O. Gutfleisch, A. Leonhardt, A. Graff, C. Taschner, and J. Fink, Appl. Phys. Lett. **80**, 2985 (2002).
[10] M. Hirscher *et al.* Appl. Phys. A: Mater. Sci. Process. **72**, 129 (2001).
[11] L. Schlapbach and A. Zuettel, Nature (London) **414**, 353 (2001).
[12] E. Barborini, P. Piseri, P. Milani, G. Benedek, C. Ducati, and J. Robertson, Appl. Phys. Lett. **81**, 3359 (2002).
[13] E. Barborini, C. Lenardi, P. Piseri, P. Milani, R.G. Agostino, T. Caruso, E. Colavita, S. La Rosa, M. Bertolo, and C. Ducati, Eur. Phys. J. D (to be published).
[14] E. Barborini, P. Piseri, and P. Milani, J. Phys. D **32**, L105 (1999).
[15] F. Ernst and M. Rühle, High-Resolution Imaging and Spectrometry of Materials (Springer-Verlag, Berlin, Heidelberg, 2003).
[16] J. Stöhr, *NEXAFS Spectroscopy* (Springer-Verlag, Berlin, Heidelberg, 1991).
[17] J. Chen, Surf. Sci. Rep. **30**, 1 (1997).
[18] H. Lüth, *Surfaces and Interfaces of Solid Materials* (Springer-Verlag, Berlin, 1996).
[19] M. D. Crescenzi and M. Piancastrelli, *Electron Scattering and Related Spectroscopies* (World Scientific, Singapore, 1996).
[20] *Materials Science of Carbides, Nitrides and Borides*, edited by Y. G. Gogotsi and R. A. Andrievski, Vol. 68 of NATO Science Series II: Mathematics, Physics and Chemistry, (Kluwer Academic Publishers, Dordrecht, 1999).
[21] L. Qian, L. Norin, J.-H. Guo, C. Såthe, A. Agui, U. Jansson, and J. Nordgren, Phys. Rev. B **59**, 12667 (1999).
[22] C. Lenardi, P. Piseri, V. Briois, C.E. Bottani, A.L. Bassi, and P. Milani, J. Appl. Phys. **85**, 7159 (1999).
[23] V.S. Lusvardi, M.A. Barteau, J.G. Chen, J.J. Eng, B. Frühberger, and A. Teplyakov, Surf. Sci. **397**, 237 (1998).
[24] F.M.F. de Groot, J.C. Fuggle, B.T. Thole, and G.A. Sawatzky, Surf. Sci. **41**, 928 (1990).
[25] R.D. Leapman, L.A. Grunes, and P.L. Fejes, Phys. Rev. B **26**, 614 (1982).
[26] T.J. Reagan, H. Ohldag, C. Stamm, F. Nolting, J. Lüning, J. Stöhr, and R.L. White, Phys. Rev. B **64**, 214422 (2001).
[27] A.E. Riedo, E. Magnano, S. Rubini, M. Sancrotti, E. Barborini, P. Piseri, and P. Milani, Solid State Commun. **116**, 287 (2000).
[28] C. Lenardi, E. Barborini, V. Briois, L. Lucarelli, P. Piseri, and P. Milani, Diamond Relat. Mater. **10**, 1195 (2001).
[29] D.E. Ramaker, CRC Crit. Rev. Solid State Mater. Sci. **17**, 211 (1991).
[30] S. Ferrer, F. Comin, J. Martin, L. Vazquez, and P. Bernard, Surf. Sci. **251–252**, 960 (1991).
[31] J.E. Houston, J.W. Rogers, Jr., R.R. Rye, F.L. Hutson, and D.E. Ramaker, Phys. Rev. B **34**, 1215 (1986).
[32] J.A. Martin-Gago, J. Fraxedas, S. Ferrer, and F. Comin, Surf. Sci. **260**, L17 (1992).
[33] G. Speranza, L. Calliari, N. Laidani, and M. Anderle, Diamond Relat. Mater. **9**, 1856 (2000).
[34] J. Schäfer, J. Ristein, R. Graupner, L. Ley, U. Stephan, T. Fruaenheim, V. Veerasamy, G.A.J. Amaratunga, M. Weiler, and H. Ehrhardt, Phys. Rev. B **53**, 7762 (1996).
[35] This feature is typically identified looking to a shoulder at 275.0 eV in the first derivative C *KVV* spectrum, see Ref. 32.
[36] J.E. Houston, D.E. Ramaker, J.W. Rogers, Jr., R.R. Rye, and F.L. Hutson, Phys. Rev. Lett. **56**, 1302 (1986).
[37] S.A. Züttel, C. Nützenadel, P. Sudan, P. Mauron, C. Emmenegger, S. Rentsch, L. Schlapbach, A. Weidenkaff, and T. Kiyobayashi, J. Alloys Compd. **330–332**, 676 (2002).
[38] M.A. Horn, J. Biener, A. Schenk, C. Lutterloch, and J. Küppers, Surf. Sci. **331–333**, 178 (1995).
[39] A. Dinger, C. Lutterloh, J. Biener, and J. Küppers, Surf. Sci. **421**, 17 (1999).
[40] K.J. Robertson and E.P. O'Reilly, Phys. Rev. B **35**, 2946 (1987).
[41] D.E. Ramaker, J. Vac. Sci. Technol. A **7**, 1614 (1989).
[42] S.D. Bader, G. Zajac, and J. Zac, Phys. Rev. Lett. **50**, 1211 (1983).
[43] E. Colavita, A. Amoddeo, R.G. Agostino, A. Bonanno, G. Chiarello, V. Formoso, and L.S. Caputi, Surf. Sci. **211–212**, 481 (1989).
[44] P. Chen, X. Wu, X. Sun, J. Lin, W. Ji, and K.L. Tan, Phys. Rev. Lett. **82**, 2548 (1999).
[45] G. Chiarello, E. Maccallini, R.G. Agostino, V. Formoso, A. Cupolillo, D. Pacilé, E. Colavita, L. Papagno, L. Petaccia, R. Larciprete, S. Lizzit, and A. Goldoni, Carbon **41**, 985 (2003).
[46] J. Yuan and L.M. Brown, Micron **31**, 515 (2000).
[47] A.C. Ferrari, A. Libassi, B.K. Tanner, V. Stolojan, J. Yuan, L.M. Brown, S.E. Rodil, B. Keinsorge, and J. Robertson, Phys. Rev. B **62**, 11 089 (2000).
[48] D. H. Ibach and D. L. Mills, *Electron Energy Loss Spectroscopy and Surface Vibrations* (Academic Press, New York, 1982).
[49] F.C. De Martino, F. Demichelis, A. Tagliaferro, M. Patrini, A. Rizzi, M. Fontane, and J. Layet, Diamond Relat. Mater. **4**, 996 (1995).
[50] S. Siebentritt, R. Pues, K.H. Rieder, and A.M. Shikin, Phys. Rev. B **55**, 7927 (1997).
[51] P. Milani *et al.* (unpublished).